JGR

RESEARCH ARTICLE

Key Points:
- Global patterns in a spaceborne methane IPDA lidar's precision are assessed
- CALIPSO and MODIS data are used for optical depth and ground reflectance
- The precision over 50×50 km^2 is 1% to 2% for key methane source regions

Correspondence to:
C. Kiemle,
Christoph.Kiemle@dlr.de

Performance simulations for a spaceborne methane lidar mission

C. Kiemle[1], S. R. Kawa[2], M. Quatrevalet[1], and E. V. Browell[3]

[1]Deutsches Zentrum für Luft- und Raumfahrt (DLR), Institut für Physik der Atmosphäre, Oberpfaffenhofen, Germany, [2]NASA Goddard Space Flight Center, Greenbelt, Maryland, USA, [3]STARSS II Affiliate, NASA Langley Research Center, Hampton, Virginia, USA

Abstract Future spaceborne lidar measurements of key anthropogenic greenhouse gases are expected to close current observational gaps particularly over remote, polar, and aerosol-contaminated regions, where actual in situ and passive remote sensing observation techniques have difficulties. For methane, a "Methane Remote Lidar Mission" was proposed by Deutsches Zentrum für Luft- und Raumfahrt and Centre National d'Etudes Spatiales in the frame of a German-French climate monitoring initiative. Simulations assess the performance of this mission with the help of Moderate Resolution Imaging Spectroradiometer and Cloud-Aerosol Lidar and Infrared Pathfinder Satellite Observations of the earth's surface albedo and atmospheric optical depth. These are key environmental parameters for integrated path differential absorption lidar which uses the surface backscatter to measure the total atmospheric methane column. Results show that a lidar with an average optical power of 0.45 W at 1.6 μm wavelength and a telescope diameter of 0.55 m, installed on a low Earth orbit platform (506 km), will measure methane columns at precisions of 1.2%, 1.7%, and 2.1% over land, water, and snow or ice surfaces, respectively, for monthly aggregated measurement samples within areas of 50×50 km^2. Globally, the mean precision for the simulated year 2007 is 1.6%, with a standard deviation of 0.7%. At high latitudes, a lower reflectance due to snow and ice is compensated by denser measurements, owing to the orbital pattern. Over key methane source regions such as densely populated areas, boreal and tropical wetlands, or permafrost, our simulations show that the measurement precision will be between 1 and 2%.

1. Introduction

An increase in methane by a factor of 2.5 since preindustrial times makes it the third most important greenhouse gas in the Earth's atmosphere after water vapor and carbon dioxide, contributing 18% of the total direct radiative forcing by long-lived anthropogenic greenhouse gases on a 100 year time horizon. Taking into account additional indirect effects, methane contributes as much as 30% of the emission-based radiative forcings [*Forster et al.*, 2007]. Besides its role as a greenhouse gas, methane is also an important player in determining the hydroxyl radical-based self cleansing capacity of the atmosphere. Moreover, it serves, through its oxidation, as an important source of stratospheric water vapor, which is also an important variable in climate change. Since the atmospheric lifetime of methane is about 10 times shorter than that of carbon dioxide, its global warming potential is about 86 times higher, and its radiative forcing is about the same, on a 20 year time horizon. Thus, reductions in its emissions would quickly diminish the rate of global warming [*Forster et al.*, 2007]. At the same time, however, natural methane sources have the potential to significantly amplify human-induced climate change, for instance due to the strong dependence of methane wetland emissions on climate, release from permafrost soils and continental shelves, and potential destabilization of methane hydrates from the ocean floors [*Kort et al.*, 2012; *Walter-Anthony et al.*, 2012; *Portnov et al.*, 2013]. While total global methane emissions from anthropogenic and natural processes at the Earth's surface are reasonably well determined [*Bergamaschi et al.*, 2013], estimates of emissions by source sector vary by up to a factor of 2, and current ground-based observational networks fail to constrain methane emissions at regional scales [*Dlugokencky et al.*, 2011].

Global satellite observations with high accuracy are required to monitor these issues and to identify changes in both anthropogenic and natural methane emissions. Passive satellite sensors measure the frequency-resolved solar backscattered radiation from the Earth's surface either with an imaging absorption spectrometer like Scanning Imaging Absorption Spectrometer for Atmospheric Chartography on Environmental Satellite or

with a Fourier transform interferometer like the Greenhouse Gases Observing Satellite. Of particular concern, using these sensors however is the inability to make measurements in the high latitudes during the winter months, leaving large areas of the globe unobserved for a considerable amount of time. The data may also be biased in regions with aerosol layers or thin cirrus clouds [*Morino et al.*, 2011] or over oceans [*Basu et al.*, 2013]. On the other hand, infrared sensors like Atmospheric Infrared Sounder and Infrared Atmospheric Sounding Interferometer are not sensitive close to the methane sources on ground due to their unfavorable weighting functions [*Xiong et al.*, 2013]. Spaceborne active remote sensing using differential absorption lidar is a new and complementary approach in the sense that it can be more sensitive near the Earth's surface, essentially has zero aerosol/cloud biases, and can measure at day and night time, e.g., in dark polar regions and also over water surfaces.

Integrated path differential absorption (IPDA) lidar uses the laser light backscatter from the Earth's surface to derive the column content of atmospheric trace gases. The use of pulsed lasers and time gating in the receiver to time (height) resolve the laser backscatter profile enables signal processing to isolate the arrival time and energy in the laser return from the Earth's surface and to exclude laser photons scattered from clouds and aerosols that generally arrive earlier. Hence, the technique allows isolating the full column trace gas measurements from potential bias errors caused by atmospheric scattering, which is a major advantage of active remote sensing. Auxiliary information includes knowledge of the absorption cross section of the spectral line probed and of the surface pressure for trace gas mixing ratio determination. Occasional ambiguities by surface pressure uncertainties or the presence of near-surface clouds can be circumvented by accurate ranging (in the order of several meters), use of a high-resolution digital elevation model, and accurate pointing knowledge. Recent studies assessed the potential of spaceborne IPDA lidars: On board a low-polar orbit satellite, this method is able to provide column carbon dioxide or methane measurements with an accuracy (systematic uncertainty; bias) of better than 1%, a precision (random uncertainty; noise) of around 1%, and global coverage between 82°S and 82°N, largely independent of aerosol load or sunlight [*Dufour and Bréon*, 2003; *Ehret and Kiemle*, 2005; *Ehret et al.*, 2008; *Amediek et al.*, 2009; *Kawa et al.*, 2010; *Kiemle et al.*, 2011]. First airborne IPDA lidar deployments recently corroborated the studies' results [*Abshire et al.*, 2014].

In contrast to measuring carbon dioxide, which most of these studies focused on and where the anthropogenic contributions are largely blurred by natural variability, the observational requirements for methane are somewhat relaxed: First, anthropogenic sources sum up to about two thirds of the total methane emissions [*Forster et al.*, 2007], which generates relatively large horizontal gradients. In addition, the shorter lifetime, and perhaps more localized sources lead to larger gradients, and fewer existing methane measurement sites all lead to less severe requirements for additional new observations to generate an impact, than with carbon dioxide. Finally, the existence of absorption line multiplets of methane, unavailable for carbon dioxide, relaxes the laser's frequency stability requirement [*Kiemle et al.*, 2011], which substantially decreases instrument cost, size, and technological risk. Consequently, a "Methane Remote Lidar Mission" (MERLIN) was proposed by Deutsches Zentrum für Luft- und Raumfahrt (DLR) and Centre National d'Etudes Spatiales (CNES) in 2010 in the frame of a German-French climate monitoring initiative [*Stephan et al.*, 2011]. The goal is to measure atmospheric methane at high precision and unprecedented accuracy sufficient to constrain the various surface sources significantly better than with the current observational network. The MERLIN mission will have a minimum operational lifetime of 3 years. It is currently in Phase B, in which all mission components are planned in detail. The launch is foreseen in 2019.

The MERLIN data will primarily be supplied to inverse numerical models [*Basu et al.*, 2013; *Bergamaschi et al.*, 2013] that use the globally observed concentration gradients to infer methane surface fluxes with a foreseen grid resolution of 1000 km and a temporal resolution of 1 month, which represents a considerable improvement from the current state of the art. The MERLIN scientific advisory group set up a list of user requirements the mission has to fulfill to meet its goal. Essentially, the lidar instrument is designed such as to obtain global methane column measurements with a random uncertainty (hereafter referred to as precision) of typically 1% for measurements aggregated at a spatial resolution of 50 km and a temporal resolution of 1 month. The systematic uncertainty (denoted accuracy) is required to be one tenth of the measurement precision, 0.1%. These uncertainties are expressed as 1 sigma errors assuming a Gaussian measurement error distribution.

Table 1. Instrument, Platform, and Environmental Parameters of the MERLIN Baseline Concept[a]

Transmitter	
Laser pulse energy	9.0 mJ
Average output power	0.45 W
Pulse repetition frequency	50 Hz
Spot diameter at mean sea level	135 m
Online wavelength	1645.552 nm
Off-line wavelength	1645.846 nm
Receiver	
Telescope diameter	0.55 m
Optical filter bandwidth	1 nm full width at half maximum
Total optical efficiency	0.65
Detector type	InGaAs Avalanche photodetectors
Quantum efficiency	0.6
Noise equivalent power	43 fW/$\sqrt{Hz}$
Platform	
Orbit type	polar, Sun synchronous, and dawn/dusk
Orbit altitude	506 km
Footprint velocity	7 km/s
Along-track resolution	50 km
Continuously available instrument power	100 W
Instrument volume	1 m^3
Instrument weight	100 kg
Environment	
Pressure and temperature	standard atmosphere profiles
Methane mixing ratio	1.774 ppmv in the troposphere [Forster et al., 2007]

[a]*Kiemle et al.* [2011] show that a methane column measurement precision of 0.8% is obtained with this set of parameters, assuming a total one-way aerosol optical depth of 0.1 and a surface backscatter reflectance of 0.1 sr^{-1} for vegetation at 1.6 μm wavelength [*Amediek et al.*, 2009].

Previous studies concentrated on the assessment of IPDA lidar accuracy [*Dufour and Bréon*, 2003; *Ehret and Kiemle*, 2005; *Ehret et al.*, 2008] and instrument parameter sensitivity [*Kiemle et al.*, 2011]. They used global average values to describe relevant parameters in the geophysical measurement environment. This paper, on the other hand, focuses on the expected spatial and seasonal variations of MERLIN's measurement precision, or random uncertainty (mainly driven by the detection noise), using an approach that for the first time aims to constrain the simulation as closely as possible to real-world conditions. The instrument model that has been developed for MERLIN [*Kiemle et al.*, 2011] is combined with existing satellite observations of the two key environmental state variables, surface albedo and optical depth, for one exemplary year. Such a detailed approach was missing in previous studies but is mandatory to assess the expected global measurement precision. We describe the results of this approach, highlighting key emission regions, and discuss limitations of the approach.

2. MERLIN Baseline

The IPDA lidar technique uses differential absorption, i.e., the difference in atmospheric transmission between a laser emission with a wavelength placed at or near the center of a methane absorption line, denoted online, and a reference off-line wavelength with no significant absorption. The instrument directs the narrow, coaligned online and off-line laser beams toward nadir and measures the energy of the laser echoes reflected from land and water surfaces. Table 1 lists the main instrument, satellite, and geophysical environment parameters of the so-called baseline concept that was used for the MERLIN Phase A studies. The current Phase B concept deviates in few parameters (larger telescope and smaller laser power) that basically compensate each other.

By positioning the online wavelength in the local methane absorption minimum or "trough" in between two strong absorption line multiplets at 1645.55 nm, the laser frequency stability requirement can be vastly relaxed, while sounding in the wings of the lines provides high near-surface measurement sensitivity [*Kiemle et al.*, 2011]. This online position also offers low temperature sensitivity. The off-line position, on the other hand, is selected such as to minimize interference by water vapor absorption line wings. The instrument's power and space demands satisfy the constraints of a small satellite that will be suitable for a "piggyback" launch on top of a larger payload, to reduce mission cost. A Sun-synchronous dawn/dusk polar orbit is favored for nearly uninterrupted solar power supply. The solar background radiance and the Earth's thermal radiation are low compared to the detector's dark current [*Kiemle et al.*, 2011]. Transmitter and receiver efficiencies assumed in the instrument model are based on previous studies and our own experience with airborne lidars.

By principle, the physical quantity measured by MERLIN is the differential atmospheric optical depth (DAOD) between online and off-line sounding frequencies, which can subsequently be converted into a weighted

average of the dry air volume mixing ratio of methane over the whole column, XCH_4, by making use of auxiliary data from numerical weather prediction models, whereby XCH_4 equals the ratio of the DAOD and the integrated atmospheric weighting function. Note that XCH_4 is not to be understood as a pure column amount but as a multifactorial result (expressed by the "X") that depends on the weighting function describing the measurement sensitivity at each height. It is nevertheless well established that such measurements can be appropriately assimilated by inverse models [see, e.g., *Basu et al.*, 2013].

Random (i.e., uncorrelated from one measurement to the next) and systematic (i.e., correlated among measurements in time and space) measurement errors may arise within the instrument itself, i.e., at DAOD level, or from uncertainties in the weighting function, i.e., at XCH_4 level. Random/systematic error sources at XCH_4 level include uncertainties in the model's surface pressure and in its temperature and water vapor profiles. As far as instrument-related systematic error sources are concerned, unknown frequency instabilities of the laser, uncertainties in the relative pulse energy monitor, and unknown spectral impurities in the laser spectrum are major contributors. Finally, since the XCH_4 data are to be assimilated by inverse models, the actual methane variability may lead to representativeness errors for models that do not assimilate single measurements in time and space, but spatially and temporally averaged data, because of the one-dimensional footprint of the instrument and of gaps in the data.

In the following paragraphs, we assume a uniform methane distribution and neglect all error sources other than the dominant random error source which drives the precision of the instrument, namely, the detection noise. The signal-to-noise ratio in the detection process is a function of the number of return photons, which in turn depends on the one hand on a number of instrument performance parameters and on the other hand on the highly variable geophysical conditions in the instrument's field of view. Concerning the latter, *Kiemle et al.* [2011] identified surface reflectance and atmospheric optical depth as being of key importance. In the absence of detailed knowledge on their variability, these environmental parameters had been kept constant to represent typical, average vegetation albedo and aerosol concentration, respectively (see footnote in Table 1). The present study closes the knowledge gap by assessing the impact of their actual variability on MERLIN's performance.

3. Model Setup

In order to estimate the global distribution of the precision of MERLIN's methane column concentration measurements, satellite observations by CALIPSO (Cloud-Aerosol Lidar and Infrared Pathfinder Satellite Observations) [*Winker et al.*, 2009] and MODIS (Moderate Resolution Imaging Spectrometer) [*Schaaf et al.*, 2002] covering the whole year 2007 are used to constrain the simulation as closely as possible to real-world conditions, in an approach similar to the works of *Kawa et al.* [2010]. Figure 1 illustrates this approach. The year 2007 was selected because it has the least losses: only about 5% of the CALIPSO data are missing mainly due to satellite maneuvers. Our instrument model uses the baseline configuration in Table 1 and essentially consists of the IPDA lidar equation with related error propagation formula detailed by *Kiemle et al.* [2011]. With reference to the auxiliary input data in Figure 1, we derived atmospheric profiles of the methane absorption cross sections at the online and off-line wavelengths from recent spectroscopic measurements [*Campargue et al.*, 2013] utilizing standard atmospheric profiles of pressure and temperature. The simulation also accounts for weak carbon dioxide and water vapor absorption lines that are close to MERLIN's online and off-line positions but negligible to the measurement precision.

3.1. Cloud and Aerosol Optical Depth

The total vertical optical depth by aerosol and cloud layers is provided by the CALIPSO mission data. CALIPSO is a dual-wavelength polarization lidar designed to acquire vertical profiles of attenuated atmospheric backscatter from a near-nadir viewing geometry during both day and night [*Winker et al.*, 2009]. We use CALIPSO as the model for the MERLIN orbital sampling. CALIPSO travels in the so-called "A-train" orbit, which is a 705 km Sun-synchronous polar orbit with an equator crossing time of about 1:30 A.M./P.M. local solar time and a 16 day repeat cycle [*L'Ecuyer and Jiang*, 2010]. The orbit inclination of 98° provides global coverage between 82°N and 82°S. MERLIN's orbit parameters and laser beam dimensions will be comparable, so that beam attenuation by aerosol and cloud cover is similar. We use the level 2 optical depths with a horizontal resolution of 5 km along the subsatellite track, which is 10 times better than MERLIN's nominal resolution of
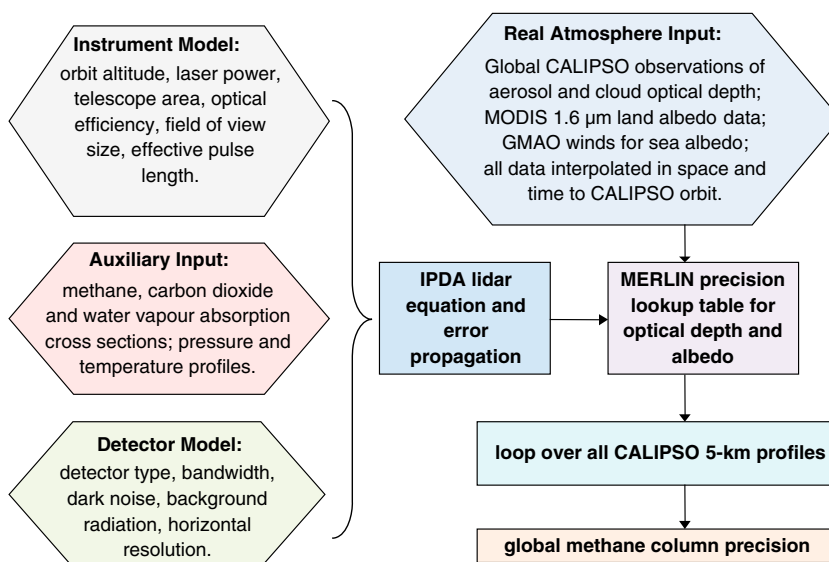
Figure 1. Schematic diagram of the model framework used to assess the MERLIN performance.

50 km (Table 1) to account for the high small-scale variability. We do not expect that MERLIN will operate in a simple along-track averaging mode; rather, cloud clearing will be done at single-shot resolution, producing a conditionally sampled or weighted measurement with optical depth significantly less than the 50 km average. Retrievals from cloud top reflection may be possible under certain conditions, but we neglect those opportunities for now.

CALIPSO cloud optical depths are reported for the 532 nm laser only, presuming that cloud extinction is largely independent of wavelength [*Vaughan et al.*, 2010]. Note that optically thin cirrus clouds that do not significantly hinder MERLIN measurements may occasionally contain particles of size down to 532 nm or smaller. In these cases, we overestimate the optical depth at 1646 nm, as extinction by such small particles decreases with increasing wavelength. To this respect, the study consequently represents a worst case assessment. Aerosol optical depths are reported at 532 and 1064 nm. We use the 1064 nm product for completeness, but for our application, the contribution of aerosol to the total attenuation is nearly negligible. Note however that regionally, the aerosol optical depth can be considerable, e.g., over the Sahara or Southeast Asia. Up to 10 layer optical depths are reported for each profile. We simply sum them all in the vertical to obtain a total (cloud and aerosol) optical depth. This method underestimates actual optical depth in opaque clouds, but we only use low optical depths. Profile samples with optical depth larger than 1 are masked out, which results in about 57% of all 5 km CALIPSO profiles in 2007 being used. This cutoff is a qualitative compromise between minimizing the random error produced at high optical depth (low signal-to-noise ratio (SNR), bad precision) and maximizing the number of accepted samples.

The probability density function (PDF) over all 4×10^7 5-km optical depths measured in 2007 is skewed, with a maximum at zero, a plateau between optical depths of 0.01 and 0.10, and an exponentially shaped decrease toward higher optical depths. The CALIPSO total optical depth is reported zero in 10% of all profiles, probably because of failing lidar inversion in case of too weak backscatter. Percentiles well describe the highly skewed distribution: for 2007, the lower (higher) decile optical depth is 0.0 (1.3), the lower (higher) quartile optical depth is 0.02 (0.34), and the median is 0.11. The values agree well with assessments in *Kiemle et al.* [2011] that were based on airborne lidar measurements over the Atlantic Ocean [*Vaughan et al.*, 1995]. We replace CALIPSO's unphysical zero optical depths by 0.01, which corresponds to the lower decile optical depth from *Kiemle et al.* [2011].

3.2. Land and Sea Surface Reflectance

The IPDA return signal strength is directly proportional to the surface reflectance, so the measurement precision depends strongly on this environmental parameter that varies widely around the globe. Reflectance at 1.6 μm is generally lower over ice and water than land, but the difference is not as large as for passive sensors since

Table 2. Overview of Relationships Utilized to Assess Backscatter Reflectance at 1.6 μm Wavelength[a]

Surface Type	GMAO Snow or Ice Fraction (f)	GMAO Wind Speed (v; m/s)	Resulting Backscatter Reflectance (β; sr^{-1})	Comment/Reference
Land				
	$f < 0.95$		$\beta = (1.23 - 0.23 \cdot f) \cdot \rho$	ρ is the MODIS 1.6 μm surface reflectance in sr^{-1}
	$f < 0.95$		$\beta = (1.23 - 0.23 \cdot f) \cdot (0.064\,\text{sr}^{-1} - 0.048\,\text{sr}^{-1} \cdot f)$	when MODIS data are missing (see text)
Snow or ice				
	$f > 0.95$		$\beta = 0.016\,\text{sr}^{-1}$	*Dumont et al.* [2010]
Water				
		$v < 1$ m/s	$\beta = 0.105\,\text{sr}^{-1}$	(Hu, private communication, 2011)
		1 m/s $< v < 7$ m/s	$\beta = \dfrac{0.00154\ \text{sr}^{-1}}{0.0146\sqrt{v}}$	*Hu et al.* [2008]
		7 m/s $< v < 13.3$ m/s	$\beta = \dfrac{0.00154\ \text{sr}^{-1}}{0.003\ +\ 0.00512v}$	*Hu et al.* [2008]
		$v > 13.3$ m/s	$\beta = 0.0213\,\text{sr}^{-1}$	*Lancaster et al.* [2005]

[a]Over land free of snow or ice, MODIS reflectances are multiplied by an enhancement factor of 1.23 after *Disney et al.* [2009], assuming a linear decrease of the enhancement factor with increasing snow/ice fraction f. Gaps are filled with reflectances and enhancement factors linearly dependent on f: if $f = 0$, an albedo of 0.2 is assumed; if $f = 1$, β equals the snow/ice reflectance. Snow/ice fraction over land and wind speed over water are determined with NASA Goddard's Global Modeling and Assimilation Office (GMAO) weather analysis interpolated in space and time to the CALIPSO/MODIS data.

the lidar continually views the glint point at nadir. Surface reflectance over land is provided by MODIS (Terra + Aqua) 5 km, 16 day composite nadir bidirectional reflectance distribution function-adjusted reflectance data at 1.64 μm (band 6; fits ideally with the MERLIN wavelengths), which are available every 8 days [*Schaaf et al.*, 2002]. The reflectances are interpolated in space and time onto the CALIPSO track to obtain a merged data set at 5 km resolution for 2007. We employ the term "reflectance" to express lidar backscatter from the Earth's surface, in units of per steradian (sr^{-1}). It is defined such that for a Lambertian surface, the albedo = reflectance $\cdot \pi \cdot$ sr.

In many situations over land surfaces, the lidar backscatter is larger than diffuse reflectance in the zenith direction, mainly because of the absence of shadows in the telescope field-of-view due to coaxial illumination of the spot by the laser. Many publications have investigated the value of this enhancement, which is called the "opposition" or "hot spot" effect. It was found to vary significantly with illumination angle, and measurements at large zenith angles are more common than at zenith angles near zero, which are more appropriate for a nadir-pointed lidar system. The publication by *Disney et al.* [2009] is one of the few that attempts to quantify the enhancement factor for a solar zenith angle near zero for a number of land cover types. In their paper, it was found to range from 1.10 to 1.33 with an average of 1.23 for six different vegetation types. Based on this work, we multiply the MODIS diffuse reflectances with an average enhancement factor of 1.23.

Table 2 gives an overview of all surface reflectance relationships applied here. For missing land data due to long-term cloud cover, we assume an albedo of 0.2, which, if divided by π, yields a reflectance of 0.064 sr^{-1}. Multiplied with the average enhancement factor of 1.23, we obtain a reflectance of 0.078 sr^{-1}. For snow and ice surfaces, we use a constant albedo of 0.05 (reflectance of 0.016 sr^{-1}) from a recent study by *Dumont et al.* [2010]. Snow/ice regions are determined from NASA Goddard's Global Modeling and Assimilation Office (GMAO) weather analysis interpolated in space and time onto the CALIPSO track. Over snow and ice, and where MODIS reflectances are missing or unrealistic (that is <0.01 sr^{-1} or >0.32 sr^{-1}), they are filled with reflectances from 0.064 sr^{-1} to 0.016 sr^{-1} and with enhancement factors from 1.23 to 1.0 with both parameters scaled based on the GMAO snow cover fraction from 0 to 0.95.

The strength of laser backscatter from a water surface from a nadir-directed laser beam depends on wind speed: while flat water surfaces in the absence of wind behave as mirrors, wavy surfaces reduce the backscatter toward the zenith. *Hu et al.* [2008] derived a functional relationship between the CALIPSO lidar
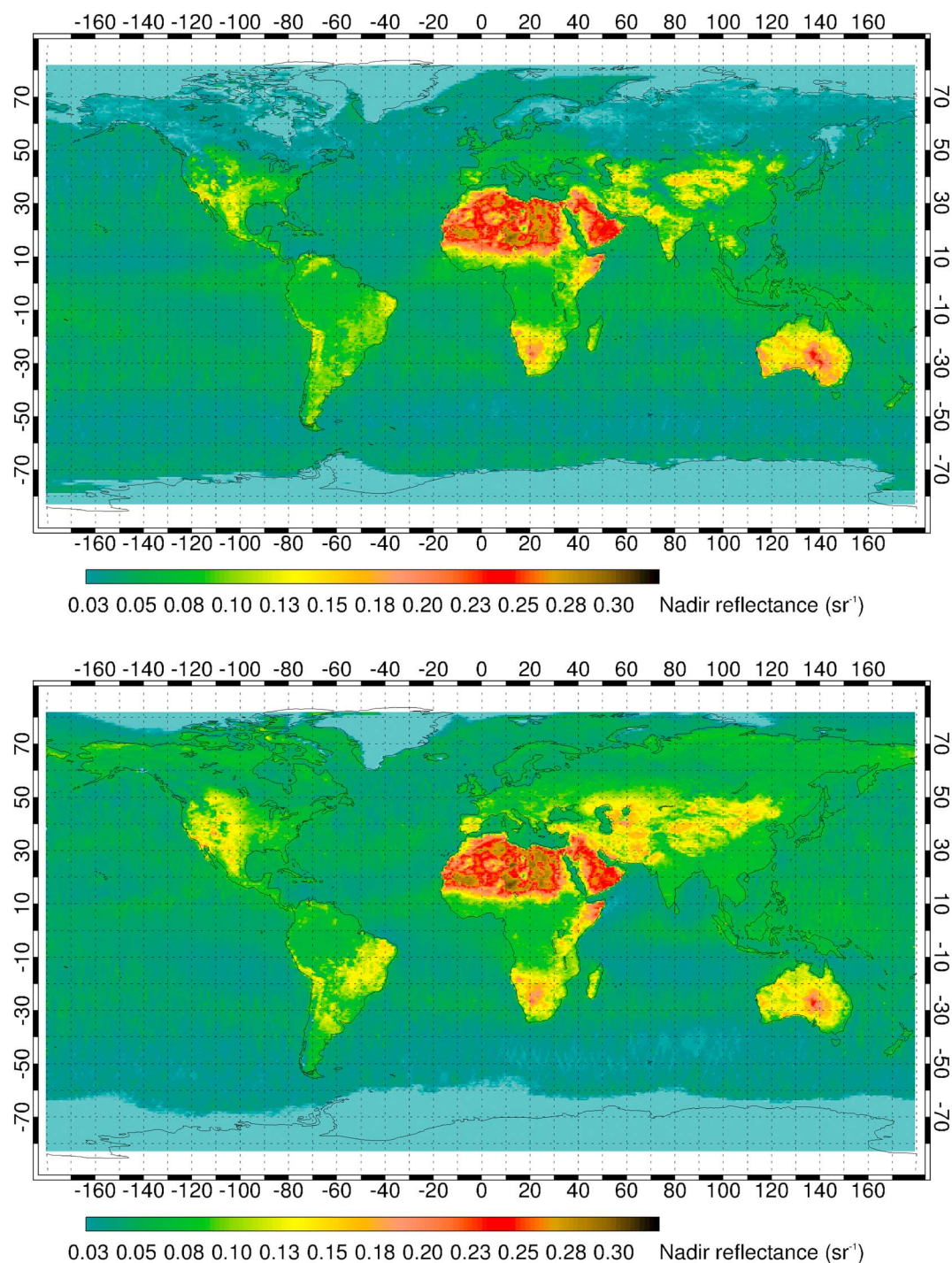
Figure 2. Global backscatter reflectances at 1.6 μm wavelength from MODIS data over land and GMAO winds over sea after Table 2 and averaged over (top) January/February/March and (bottom) July/August/September 2007. The winter-summer contrast is clearly seen, mainly through a latitudinal wind zone shift over the oceans and different snow cover over the northernmost land surfaces.

backscatter measurements at 1064 nm and surface wind speed measurements, given in Table 2. We use this relationship with the GMAO 10 m winds interpolated in space and time onto the CALIPSO track. For wind speeds above 13.3 m/s, where there can be a mixture of white caps and foam on the sea surface, we use a constant surface backscatter equal to the backscatter at 13.3 m/s. This approach is consistent with the results
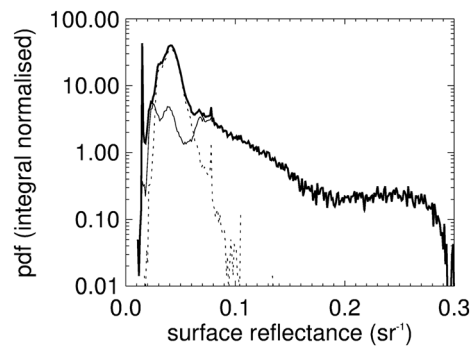
Figure 3. Probability distribution function of surface reflectance at 1.6 μm wavelength, computed using MODIS data over land (thin solid line) and GMAO winds over sea (thin dotted, see Table 2), for the whole year 2007.

of *Lancaster et al.* [2005], which only had one data point at ~16 m/s, and its value was nearly the same as that at 13.3 m/s. In addition, it is believed that these equations can be used down to very low wind speeds due to the relatively large size of the laser footprint (of order 100 m) and the ubiquitous nature of low-frequency gravity waves on most large water surfaces (e.g., oceans and Great Lakes). For these conditions, it is estimated by Hu (private communication, 2011) that the backscatter would peak at a wind speed value of about 1 m/s.

Figure 2, the resulting global surface reflectance map for winter and summer 2007, shows high spatial and seasonal variability, in particular between land and ocean, and over the northernmost land surfaces due to varying snow cover. Other regions, such as central Asia and South America, exhibit slightly higher reflectance in (northern) summer. Significant spatial variability by up to a factor of two is observed between semiarid and fully vegetated surfaces. Deserts also exhibit strong variability at highest reflectances but are not that relevant for MERLIN, except for instrument calibration purposes. Over the oceans, longitudinal bands with more reflectance, belonging to calm regions, alternate with regions of stronger winds that reflect less, especially around 50°S. The maps are 3 month averages of 1×10^7 5-km data computed using the relationships in Table 2, interpolated onto the CALIPSO track, and binned into quadratic tiles of size 50×50 km^2. The resulting PDF of surface reflectance in Figure 3 shows a distinct peak at 0.016 sr^{-1} due to the assumption of a constant value for snow/ice surfaces, a broader peak mainly from water surfaces around 0.04 sr^{-1}, and a smooth transition toward higher but less frequent reflectances over land. The plateau between 0.18 and 0.28 sr^{-1} belongs to deserts, the red/brown areas in Figure 2. The tiny peak at 0.078 sr^{-1} is caused by our fill value for MODIS data gaps, as mentioned above. The ratio between maxima over arid land (~0.3 sr^{-1}) and lowest reflectances over snow/ice surfaces (0.016 sr^{-1}) is about 20. It determines the dynamic range of MERLIN's surface backscatter signals and is important for the design of the detector and signal chain.

Table 3 shows that the mean land reflectance at 1.6 μm wavelength in 2007 was 0.08 sr^{-1}, which corresponds to an albedo of 0.20 for Lambertian surfaces without enhancement factor. In summer, the reflectance was 20% higher than this full year average, mainly because of the absence of snow in the northern hemisphere (see also Figure 2). Since water surfaces dominate the PDF, the global median reflectance of 0.04 sr^{-1} equals the arithmetic mean reflectance over sea. Both do not vary between winter and summer. The lower and higher deciles, indicating cumulative probabilities of 10 and 90%, mirror the slight reflectance increase in summer over land. In 2007, their ratio amounts to 3, which expresses the high variability of surface reflectance.

Table 3. Global Backscatter Reflectances for the Year 2007 at 1.6 μm Wavelength, Computed With MODIS Data Over Land and GMAO Winds Over Sea After Table 2[a]

Surface Type	Jan/Feb/Mar	Jul/Aug/Sep	Whole 2007
Land mean	0.083 sr^{-1}	0.098 sr^{-1}	0.083 sr^{-1}
Sea mean	0.042 sr^{-1}	0.042 sr^{-1}	0.042 sr^{-1}
Ice/snow mean	0.016 sr^{-1}	0.016 sr^{-1}	0.016 sr^{-1}
Global median	0.041 sr^{-1}	0.044 sr^{-1}	0.043 sr^{-1}
Global higher decile	0.09 sr^{-1}	0.10 sr^{-1}	0.09 sr^{-1}
Global lower decile	0.02 sr^{-1}	0.03 sr^{-1}	0.03 sr^{-1}

[a]Land surfaces reflect about twice as much as the sea (arithmetic means), and the summer/winter contrast is generally small. Due to the skewed global distribution (see Figure 2), percentiles are used: 10% of all surfaces have a reflectance lower than 0.03 sr^{-1} (the lower decile), and 10% have a reflectance higher than 0.09 sr^{-1} (higher decile, whole 2007).
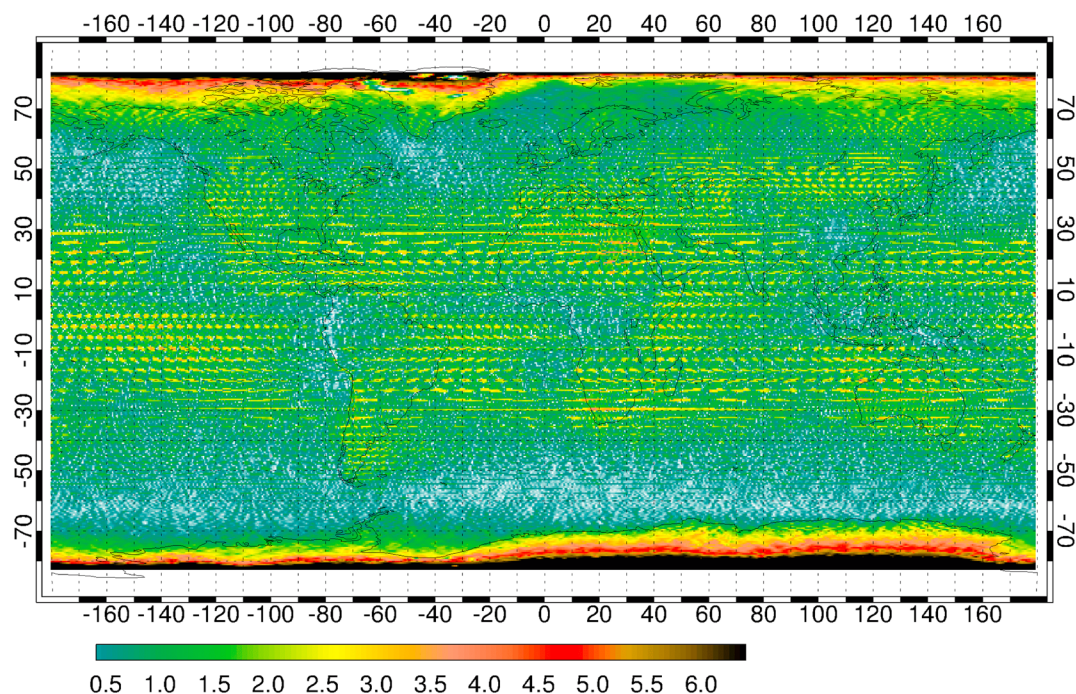
Figure 4. Number of MERLIN measurements per month and 50×50 km^2 area using the 2007 CALIPSO data. The number mainly depends on cloud cover and increases at latitudes $>70°$, where ascending and descending orbits overlap. Interference patterns are due to differences between our 50 km grid and the diamond-shaped orbital footprint. With 23.5% of the empty 50×50 km^2 tiles (too small to display on this map and hence interpolated with nonzero neighbors), the global average is only 1.8 measurements per tile and month.

4. Simulation Results

Given MERLIN's foreseen along-track resolution of 50 km (Table 1), it is advantageous for the simulation to partition the Earth's surface into quadratic tiles of 50×50 km^2 between 82°S and 82°N. This is the spatial resolution and domain of the simulation results presented in this section. However, the measurements' precision is initially computed on the high-resolution 5 km CALIPSO and MODIS grids in order to retain most of the small-scale variability in optical depth and surface reflectance. At that resolution, the 95% of useful CALIPSO data represent 4×10^7 5-km points for the year 2007. We hence use a two-dimensional lookup table to speed up the computational effort, running chronologically along CALIPSO's orbit within a time span of 1, 3, or 12 months. The lookup table relates the MERLIN measurement precision to the satellite observations of optical depth and surface reflectance, representing all encountered environmental states and using the baseline instrument configuration in Table 1 for all other parameters (see also Figure 1).

The 50×50 km^2 tiles are consecutively filled with the 5 km precision results, and after each month, a weighted average of the aggregated samples is calculated within each tile, complying with MERLIN's required spatial and temporal resolutions. The weights are inversely proportional to the 5 km measurement uncertainty and ensure that measurements with small uncertainty, e.g., in clear sky or over highly reflecting surfaces, dominate the tile average. This approach will resemble the adaptive, context-sensitive averaging of MERLIN's real measurements. Note that for this analysis, we have made the simplifying assumption that each MERLIN measurement made in a 50×50 km^2 tile over a month is sampling the same methane conditions such that we can combine the measurements and their uncertainties based on Gaussian statistics. In reality, however, the averages obtained by aggregation of individual samples are not equal to the average methane concentration over space (50×50 km^2) and time (1 month) because of small-scale variability and the small number of samples. The MERLIN results will therefore have to be compared with, or assimilated into models as directly in space and time as possible, in order to minimize sampling or representativeness uncertainties. In fact, we believe that the highest-resolution measurements (5 km or better) with their associated uncertainties should be used directly rather than even further averaging them along the track
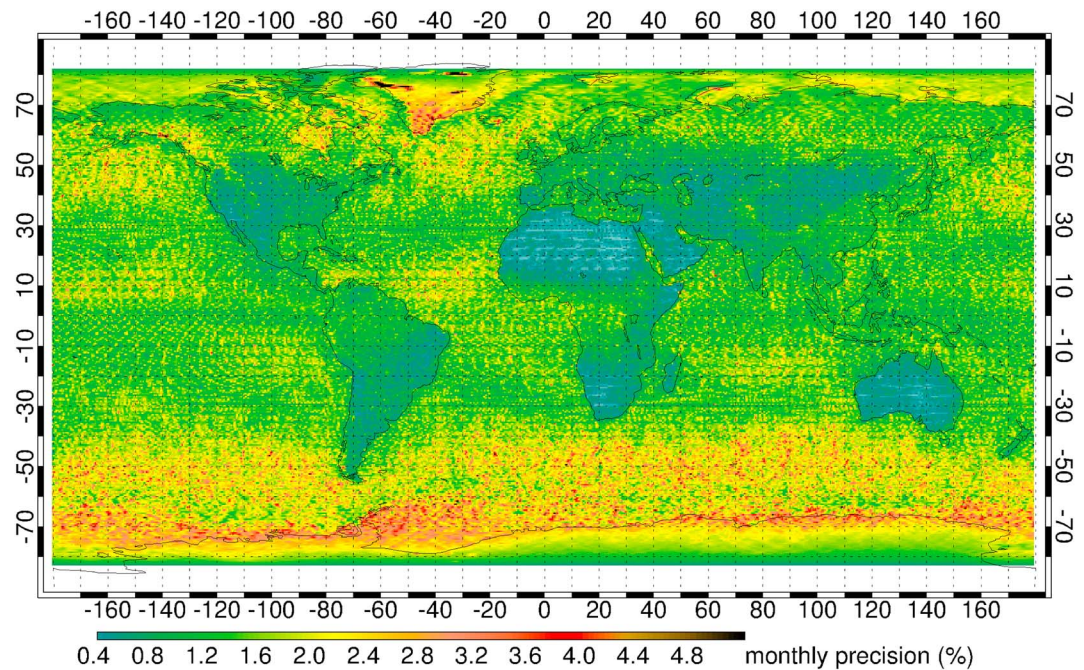
Figure 5. Simulated global distribution of the MERLIN measurement precision (random uncertainty), for monthly weighted averages of aggregated samples over 50×50 km^2 areas using a composite database of CALIPSO cloud/aerosol optical depths and MODIS/GMAO reflectances for 2007. The variability is mainly due to surface reflectance (cf. Figure 2), as fluctuations by clouds average out in this yearly view (except in continuously cloudy regions). Globally, higher reflectances lead to a considerably better performance over land. Important methane source regions such as boreal and tropical wetlands, permafrost regions, or densely populated areas are measured with 1 to 2% precision. Low reflectance due to long-duration snow cover north of 60°N is well compensated by denser measurements (cf. Figure 4).

with the above approach. This will allow the models to average these data in ways that cannot be done without a priori knowledge of the horizontal gradient in the methane fields.

Since the individual 5 km measurements are uncorrelated, we can use the Bienaymé equation, $\sigma^2(\Sigma x_i) = \Sigma(\sigma_i^2)$, to obtain the precision of a weighted average of a set of 5 km measurements sampled within 50×50 km^2 and 1 month. Using CALIPSO's orbit, a maximum optical depth of 1, and a 5 km precision cutoff of 20%, there will be, on global average 1.8 MERLIN measurements within 50 x 50 km^2 and 1 month. This equals a total of approximately 166,600 measurements/month, or 5553/day. Figure 4 shows the resulting global variability of
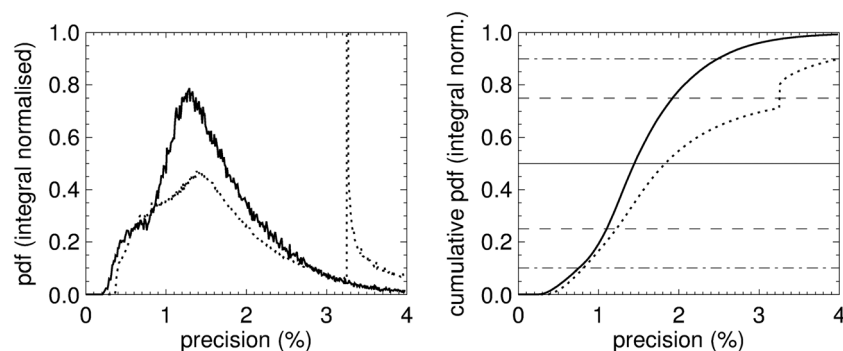

Figure 6. (left) Probability distribution function and cumulative PDF of the measurement precision of Figure 5, i.e., for monthly weighted averages of aggregated samples over 50×50 km^2 areas (solid). The distribution is close to Gaussian and has a standard deviation of 0.7% and a mean of 1.6%. MERLIN precision of 50 km along-track measurements without areal and temporal averaging, for comparison (dotted). The peak at 3.3% is due to a large number of points in clear air over snow/ice, where MODIS data are lacking and the absence of compensation by areal averaging.

Table 4. Global MERLIN Measurement Precision (Random Uncertainty) for the Simulation Year 2007, for Monthly Weighted Averages of Aggregated Samples Over Areas of $50 \times 50 \, km^2$, Using CALIPSO Cloud/Aerosol Optical Depths and MODIS/GMAO Reflectances (See Also Figures 5 and 6)[a]

Surface Type	Jan/Feb/Mar	Jul/Aug/Sep		Full Year 2007
	Monthly Averages of Aggregated Samples Over $50 \times 50 \, km^2$			50 km Along-Track Averages
Land	1.4%	1.1%	1.2%	1.4%
Sea	2.0%	2.0%	1.7%	2.0%
Snow/Ice	2.2%	2.7%	2.1%	4.3%
Global mean	1.8%	1.8%	1.6%	2.4%
Median	1.5%	1.5%	1.5%	1.8%
Higher decile	3.2%	3.2%	2.5%	4.0%
Lower decile	0.8%	0.7%	0.8%	0.8%

[a]Summer performance over land is nearly twice as good as over sea, yet on a global perspective, the summer/winter contrast is balanced. Right column: MERLIN precision of 50 km along-track measurements without areal and temporal averaging, for comparison. The values are higher, particularly over polar regions with snow/ice cover.

the measurement density, taking into account the orbit coverage, as well as losses by opaque clouds or too low surface reflectance, both identified by the performance simulation. Note that the optical depth and precision cutoffs are not required when applying weighted averages, because measurements beyond these limits, i.e., with low SNR, inherently would obtain very low weights. The cutoffs just help prevent computation errors, e.g., when a tile is fully cloud covered over a whole month. Assuming Gaussian statistics, the expression for the variance σ^2 of an average over n uncorrelated measurements x_i with weights a_i and precisions σ_i is

$$\sigma^2 \left(\frac{\sum a_i x_i}{\sum a_i} \right) = \frac{\sum a_i^2 \sigma_i^2}{\left(\sum a_i \right)^2}$$

As stated above, the weights are set inversely proportional to the n individual 5 km precisions: $a_i = 1/\sigma_i$. Note that $n = 18$ on global average. The precision of the weighted average of n samples within $50 \times 50 \, km^2$ and 1 month, expressed as a standard deviation, consequently is

$$\sigma = \frac{\sqrt{n}}{\sum 1/\sigma_i}.$$

In case all n errors σ_i are equal, $\sigma = \sigma_i/\sqrt{n}$, the standard deviation of the (nonweighted) average of n uncorrelated samples. Figures 5 and 6 both show the resulting global distribution of MERLIN's measurement precision for 2007. The best performance ($<0.5\%$) in terms of measurement precision is found over subtropical deserts due to the cloud-free and arid (high reflectance) environment. The worst performance is over sea surfaces between ~40 and 70°N (~2% average precision), Greenland (1 to 5%), and particularly south of 40°S (~3% on average), where high cloud cover and high winds prevail. Important methane source regions such as boreal and tropical wetlands, permafrost regions, or densely populated areas are expected to be measured with intermediate performance (1 to 2% precision), which satisfies the requirements defined by future users. The 16 day CALIPSO repeat cycle leads to a maximum orbit footprint spacing at the equator of about 1.5° in longitude (170 km). This gives about 23% empty $50 \times 50 \, km^2$ tiles between 82°N and 82°S, particularly around the equator where the cover is worst. They are interpolated with nonzero neighbors in Figures 4 and 5. A weak interference pattern due to differences between the 50 km data grid and the diamond-shaped orbital footprint appears over rather homogeneous regions in the tropical Pacific and Atlantic. It is blurred over the Indian Ocean and over land where optical depths and surface reflectances are more variable.

Table 5. MERLIN Horizontal Measurement Resolution Required to Obtain a Monthly Precision of 1%, From Figure 7[a]

Surface Type	Jan/Feb/Mar	Jul/Aug/Sep	Whole 2007	Fraction
Land	61 km	50 km	59 km	30.7%
Sea	79 km	80 km	77 km	63.7%
Snow/Ice	104 km	123 km	107 km	5.6%
Global mean	76 km	76 km	74 km	

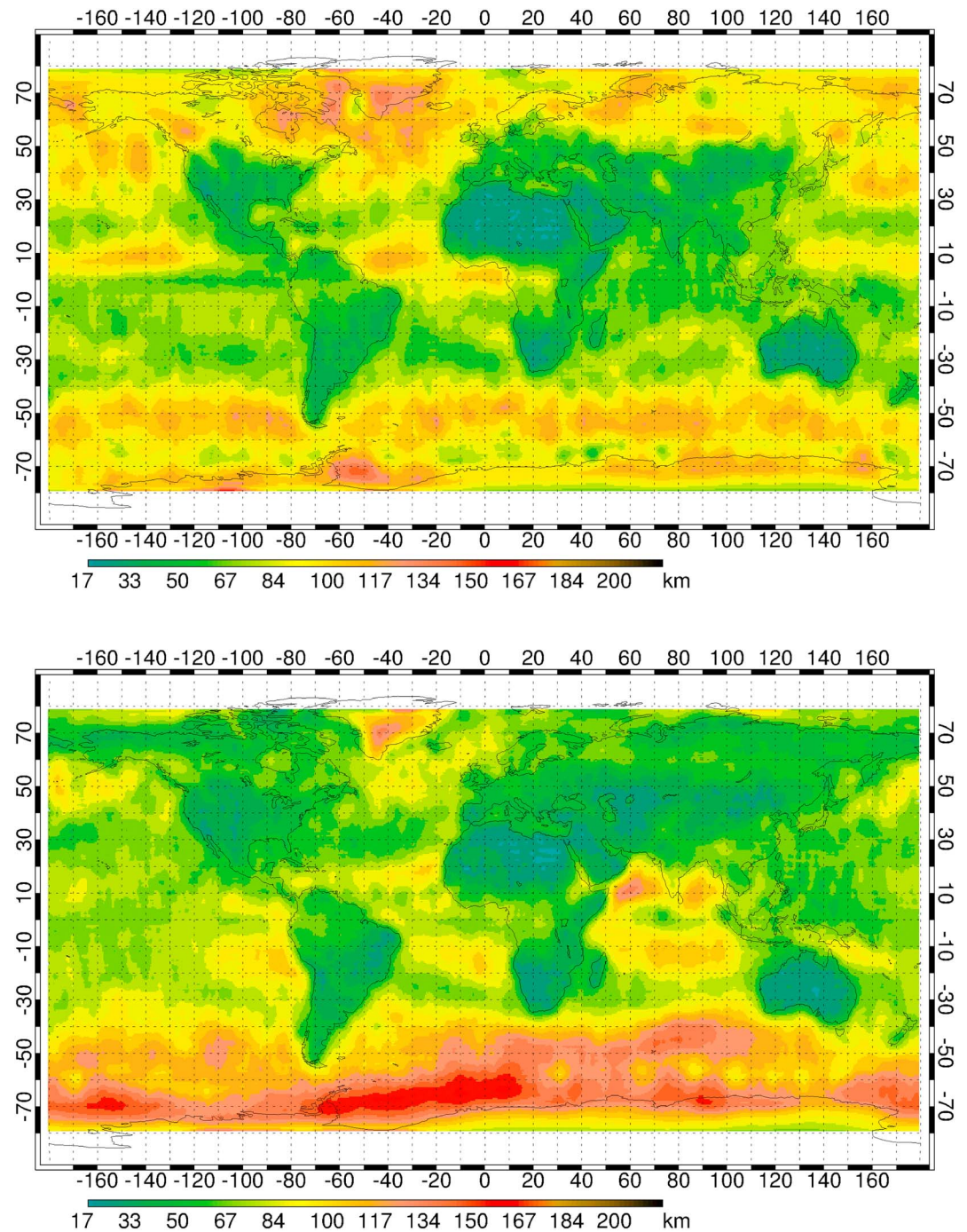[a]Right column: areal fraction of global cover from GMAO data.

Figure 7. Simulated MERLIN horizontal measurement resolution required to obtain a monthly precision of 1%, for (top) January/February/March and (bottom) July/August/September 2007. The winter-summer contrast is clearly seen, mainly through a latitudinal wind zone shift over the oceans and different snow cover over the northernmost land surfaces. See also Figure 2 and tables for comparison.

Table 4 complements Figure 5 with global precision values for summer, winter, and full 2007. While the performance over land is about 30% (100%) better than over sea (snow/ice), the summer-winter contrast is low on a global perspective. Less snow in (northern) summer improves the land performance by about 30%. Table 4 also presents the MERLIN precision of 50 km along-track measurements without further tile averaging, for comparison. The values are higher as expected, particularly over polar regions with snow/ice

cover, where areal averaging has a high potential to improve the precision due to high-measurement density (cf. Figure 4).

Future MERLIN users may be more interested to obtain monthly measurements at a constant precision of 1% for instance. Appropriately extending or reducing the $50 \times 50\,km^2$ tiles enables to accumulate as many individual, weighted 5 km measurements as needed to meet the given precision threshold, assuming as above identical methane conditions within extended tiles. The resulting spatial resolution, corresponding to the size of the adjusted area, is shown in Table 5 and Figure 7. Here also, some regions reveal a distinct winter-summer contrast, mainly from differences in snow and cloud cover, particularly over the northernmost land surfaces, the North Atlantic, the Indian Ocean, and south of 40°S. There is a proportionality between Tables 4 and 5 (and Figures 5 and 7), as the ratio of their respective values is constant and amounts to 50 km/1%. Slight deviations are due to different weighted averaging.

5. Discussion of Uncertainties

With the use of CALIPSO as model for the MERLIN orbital sampling, some differences exist with respect to the orbit foreseen for MERLIN. While the resulting footprint pattern will be similar, CALIPSO's position is 200 km higher, and CALIPSO's 1:30 A.M./P.M. local equator crossing time is 4:30 h ahead of MERLIN's dawn/dusk orbit (6:00 A.M./P.M.). This entails a slight difference in the observed cloud cover since, for example, low-level morning fog observed by MERLIN will likely have disappeared at the time of CALIPSO's overpass, whereas CALIPSO encounters more convective clouds at 1:30 P.M. than MERLIN at 6 P.M. Thus, regional differences, depending on climate zone and season, are expected. The effect on the MERLIN measurement performance is difficult to quantify as actually no CALIPSO-like lidar operates on a dawn/dusk orbit. A comprehensive assessment based on different satellite observations reveals that over oceans, there is up to 3% more cloud cover in the morning than in the early afternoon, on global average [*Stubenrauch et al.*, 2012]. Over land, their data are not conclusive, because uncertainties in cloud cover determination as well as regional and seasonal variations are relatively large. Here the morning-afternoon differences span across ±7%.

Other uncertainties in our method are easier to quantify. For example, we assume a constant tropospheric methane mixing ratio (Table 1), while actually the northern hemisphere (53 to 90°N) has about 7% higher concentrations than the southern hemisphere (53 to 90°S) [*Dlugokencky et al.*, 2011]. The resulting north/south deviation from the global mean of ±3.5% does not significantly influence our results: the simulation shows that the measurement precision is generally independent on the methane column content for the baseline configuration. Pressure and temperature variations as observed between different climates in the atmosphere also have negligible influence on the resulting precision estimation, as already shown by *Ehret et al.* [2008]. This justifies the use of standard profiles.

Furthermore, simulations by *Kiemle et al.* [2011] have shown that the measurement precision of the MERLIN baseline configuration (Table 1) is insensitive to atmospheric pressure variations for surface altitudes between 0 and 3 km. They report a precision loss due to less measurement sensitivity of about 25% and 50% for surface altitudes of 4 and 5 km, occurring over only 0.5% and 0.1% of the global area covered by MERLIN, respectively. As mountains will also likely be rejected for other reasons, e.g., steep slopes, this height effect has not been considered here. Finally, minor uncertainties in random error estimations arise from the simplifying assumptions that the environmental parameters, snow/ice albedo and enhancement factor, are globally constant, as more precise global nadir observations at 1.6 μm are lacking.

6. Conclusions and Outlook

In the frame of a German-French climate monitoring initiative, a Methane Remote Lidar Mission was proposed by DLR and CNES in 2010. The goal is to measure methane with a precision and accuracy sufficient to constrain the various surface sources significantly better than with the current observational network. Simulations of the expected measurement performance are needed to tailor the mission to the user requirements. The presented approach aims to constrain the simulation as closely as possible to real-world conditions. MODIS and CALIPSO satellite observations of the two key environmental state variables for IPDA lidar, surface albedo and optical depth, are employed to assess the impacts of their spatial and seasonal variations onto the precision (random uncertainty) of the methane measurements. This approach confirms that the baseline instrument concept established in previous studies is suitable for a successful mission, since
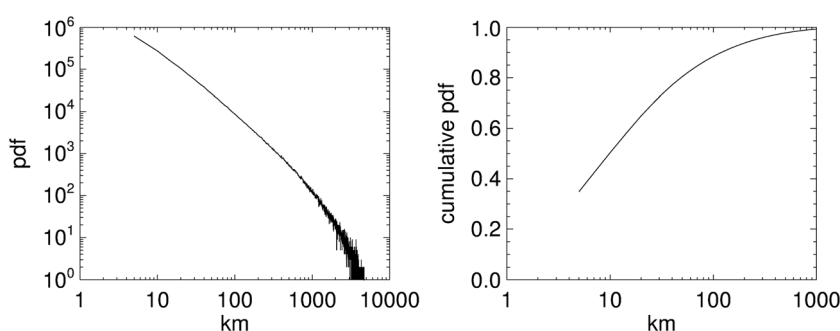
Figure 8. (left) PDF and cumulative PDF of cloud gap (i.e., clear-sky region) size using the global 5 km CALIPSO optical depths at a cutoff of 1, for the whole year 2007. Small gaps are most likely, and the median cloud gap size is 10 km.

the basic user requirements (1% precision/50 km resolution/1 month average) are globally fulfilled over land, using the year 2007 as database. Water, snow, and ice surfaces lead to a performance degradation of about a factor of 2, mainly due to their poor reflectance at 1.6 μm wavelength.

In order to better constrain the regional methane fluxes, more precise measurements are required over key source regions, such as densely populated areas, boreal and tropical wetlands, and permafrost. Our simulations show that in such hot spot regions, MERLIN is expected to measure at a precision between 1 and 2%. The present study masks out all profiles with total optical depth larger than 1 and does not exploit laser return signals from cloud tops. *Ehret et al.* [2008] showed that reflectances from tops of water clouds with optical depth >5 are large enough to be used if the cloud boundary is sharp. Such signals could give partial vertical methane column contents down to the top of the clouds, which would be of particular value wherever the cloud tops are at low level. In a broken cloud environment with interspersed total column measurements down to the Earth's surface, vertical profiles of the methane concentration could be derived by subtracting the partial columns from the total.

Another future focus will be cloud gap statistics based on CALIPSO cloud measurements. In the 2007 data used here, clouds with optical depth larger than 1 cover about 43% of the globe. The size distribution of the remaining 57% of "cloud gaps" is displayed in Figure 8. Note that the "gaps" defined this way may contain thin clouds or aerosol layers with optical depth <1. Their distribution is strongly skewed toward small scales and roughly obeys a power law with exponent of around −5/3 on scales between 5 and 1000 km. The cumulative PDF reveals that only about 20% of all gaps are larger than the nominal MERLIN resolution (50 km) and that all smallest 5 km gaps alone represent more than one third of the total number of gaps. Therefore, cloud avoidance and cloud top signal exploitation will be major issues for MERLIN as well as other spaceborne lidar projects.

References

Abshire, J. B., A. Ramanathan, H. Riris, J. Mao, G. R. Allan, W. E. Hasselbrack, C. J. Weaver, and E. V. Browell (2014), Airborne measurements of CO_2 column concentration and range using a pulsed direct-detection IPDA lidar, *Remote Sens.*, *6*, 443–469, doi:10.3390/rs6010443.

Amediek, A., A. Fix, G. Ehret, J. Caron, and Y. Durand (2009), Airborne lidar reflectance measurements at 1.57 μm in support of the A-SCOPE mission for atmospheric CO_2, *Atmos. Meas. Tech.*, *2*, 755–772.

Basu, S., et al. (2013), Global CO2 fluxes estimated from GOSAT retrievals of total column CO2, *Atmos. Chem. Phys.*, *13*, 8695–8717, doi:10.5194/acp-13-8695-2013.

Bergamaschi, P., et al. (2013), Atmospheric CH4 in the first decade of the 21st century: Inverse modeling analysis using SCIAMACHY satellite retrievals and NOAA surface measurements, *J. Geophys. Res. Atmos.*, *118*, 7350–7369, doi:10.1002/jgrd.50480.

Campargue, A., O. Leshchishina, D. Mondelain, S. Kassi, and A. Coustenis (2013), An improved empirical line list for methane in the region of the $2\nu_3$ band at 1.66 μm, *J. Quant. Spectros. Radiat. Transfer*, *118*, 49–59.

Disney, M. I., P. E. Lewis, M. Bouvet, A. Prieto-Blanco, and S. Hancock (2009), Quantifying surface reflectivity for spaceborne lidar via two independent methods, *IEEE Trans.Geosci Remote Sens.*, *47*, 3262–3271, doi:10.1109/TGRS.2009.2019268.

Dlugokencky, E. J., E. G. Nisbet, R. Fisher, and D. Lowry (2011), Global atmospheric methane: Budget, changes and dangers, *Phil. Trans. R. Soc. A*, *369*, 2058–2072, doi:10.1098/rsta.2010.0341.

Dufour, E., and F.-M. Bréon (2003), Spaceborne estimate of atmospheric CO_2 column by use of the differential absorption method: Error analysis, *Appl. Opt.*, *42*(18), 3595–3609.

Dumont, M., O. Brissaud, G. Picard, B. Schmitt, J.-C. Gallet, and Y. Arnaud (2010), High accuracy measurements of snow bidirectional reflectance distribution function at visible and NIR wavelengths - comparison with modeling results, *Atmos. Chem. Phys.*, *10*, 2507–2520.

Ehret, G. and C. Kiemle (2005), Requirements Definition for Future DIAL Instruments. Final Report, ESA Study CR(P)-4513, Contract 10880/03/NL/FF.

Ehret, G., C. Kiemle, M. Wirth, A. Amediek, A. Fix, and S. Houweling (2008), Space-borne remote sensing of CO_2, CH_4, and N_2O by integrated path differential absorption lidar: A sensitivity analysis, *Appl. Phys. B*, *90*, 593–608, doi:10.1007/s00340-007-2892-3.

Forster, P., et al. (2007), Changes in atmospheric constituents and in radiative forcing, in *Climate Change 2007: The Physical Science Basis. Contribution of Working Group I to the Fourth Assessment Report of the Intergovernmental Panel on Climate Change*, edited by S. Solomon et al., pp. 996, Cambridge Univ. Press, Cambridge, U. K., and New York.

Hu, Y., et al. (2008), Sea surface wind speed estimation from space-based lidar measurements, *Atmos. Chem. Phys.*, *8*, 3593–3601.

Kawa, S. R., J. Mao, J. B. Abshire, G. J. Collatz, X. Sun, and C. J. Weaver (2010), Simulation studies for a space-based CO_2 lidar mission, *Tellus B*, doi:10.1111/j.1600-0889.2010.00486.x.

Kiemle, C., M. Quatrevalet, G. Ehret, A. Amediek, A. Fix, and M. Wirth (2011), Sensitivity studies for a space-based methane lidar mission, *Atmos. Meas. Tech.*, *4*, 2195–2211, doi:10.5194/amt-4-2195-2011.

Kort, E. A., et al. (2012), Atmospheric observations of Arctic Ocean methane emissions up to 82° north, *Nat. Geosci.*, *5*, doi:10.1038/NGEO1452.

Lancaster, R. S., J. D. Spinhirne, and S. P. Palm (2005), Laser pulse reflectance of the ocean surface from the GLAS satellite lidar, *Geophys. Res. Lett.*, *32*, L22S10, doi:10.1029/2005GL023732.

L'Ecuyer, T. S., and J. H. Jiang (2010), Touring the atmosphere aboard the A-Train, *Phys. Today*, *63*(7), 36–41, doi:10.1063/1.3463626.

Morino, I., et al. (2011), Preliminary validation of column-averaged volume mixing ratios of carbon dioxide and methane retrieved from GOSAT short-wavelength infrared spectra, *Atmos. Meas. Tech.*, *4*, 1061–1076, doi:10.5194/amt-4-1061-2011.

Portnov, A., A. J. Smith, J. Mienert, G. Cherkashov, P. Rekant, P. Semenov, P. Serov, and B. Vanshtein (2013), Offshore permafrost decay and massive seabed methane escape in water depths >20 m at the South Kara Sea shelf, *Geophys. Res. Lett.*, *40*, 3962–3967, doi:10.1002/grl.50735.

Schaaf, C. B., et al. (2002), First operational BRDF, albedo and nadir reflectance products from MODIS, *Remote Sens. Environ.*, *83*, 135–148.

Stephan, C., M. Alpers, B. Millet, G. Ehret, P. Flamant, and C. Deniel (2011), MERLIN: A space-based methane monitor, in *Proc. SPIE, Lidar Remote Sensing for Environmental Monitoring XII*, vol. 8159, edited by U. N. Singh, pp. 815–908, San Diego, Calif., doi:10.1117/12.896589. [Available at http://proceedings.spiedigitallibrary.org/proceeding.aspx?articleid=1342709.]

Stubenrauch, C., W. Rossow, and S. Kinne (2012), Assessment of Global Cloud Data Sets from Satellites. A Project of the World Climate Research Programme Global Energy and Water Cycle Experiment (GEWEX) Radiation Panel. November 2012. WCRP Report No. 23/2012. [Available at http://www.wcrp-climate.org/documents/GEWEX_Cloud_Assessment_2012.pdf.]

Vaughan, J. M., D. W. Brown, C. Nash, S. B. Alejandro, and G. G. Koenig (1995), Atlantic atmospheric aerosols studies 2. Compendium of airborne backscatter measurements at 10.6 μm, *J. Geophys. Res.*, *100*(D1), 1043–1065.

Vaughan, M. A., Z. Liu, M. J. McGill, Y. Hu, and M. D. Obland (2010), On the spectral dependence of backscatter from cirrus clouds: Assessing CALIOP's 1064 nm calibration assumptions using cloud physics lidar measurements, *J. Geophys. Res.*, *115*, D14206, doi:10.1029/2009JD013086.

Walter-Anthony, K. M., P. Anthony, G. Grosse, and J. Chanton (2012), Geologic methane seeps along boundaries of Arctic permafrost thaw and melting glaciers, *Nat. Geosci.*, *5*, doi:10.1038/NGEO1480.

Winker, D. M., M. A. Vaughan, A. Omar, Y. Hu, K. A. Powell, Z. Liu, W. H. Hunt, and S. A. Young (2009), Overview of the CALIPSO mission and CALIOP data processing algorithms, *J. Atmos. Oceanic Technol.*, *26*(11), 2310–2323, doi:10.1175/2009JTECHA1281.1.

Xiong, X., C. Barnet, E. S. Maddy, A. Gambacorta, T. S. King, and S. C. Wofsy (2013), Mid-upper tropospheric methane retrieval from IASI and its validation, *Atmos. Meas. Tech.*, *6*, 2255–2265, doi:10.5194/amt-6-2255-2013.